

Frictional contact between solids: A fully Eulerian phase-field approach

Flavio Lorez^a, Mohit Pundir^{a,*}

^a*Institute for Building Materials, ETH Zurich, Switzerland*

Abstract

Recent advancements have demonstrated that fully Eulerian methods can effectively model frictionless contact between deformable solids. Unlike traditional Lagrangian approaches, which require contact detection and resolution algorithms, the Eulerian framework utilizes a single, fixed spatial mesh combined with a diffuse interface phase-field approach, simplifying contact resolution significantly. Moreover, the Eulerian method is well-suited for developing a unified framework to handle multiphysical systems involving growing bodies that interact with a constraining medium. In this work, we extend our previous methodology to incorporate frictional contact. By leveraging the intersection of the phase fields of multiple bodies, we define normal and tangential penalty force fields, which are incorporated into the linear momentum equations to capture frictional interactions. This formulation allows independent motion of each body using distinct velocity fields, coupled solely through interfacial forces arising from contact and friction. We thoroughly validate the proposed approach through several numerical examples. The method is shown to handle large sliding effortlessly, accurately capture the stick-slip transition, and preserve history-dependent energy dissipation, offering a solution for modeling frictional contact in Eulerian models.

Keywords: Contact mechanics, Phase-field model, Eulerian formulation

1. Introduction

Interfacial interactions are not only fundamental in various mechanical systems, ranging from engineering materials to natural phenomena, but also play a pivotal role in multiphysical processes, where they often arise as a consequence of other mechanisms and, in turn, influence these underlying processes. For instance, in biofilms, frictional contact and adhesion between growing bacterial colonies play a crucial role in the emergence of complex pattern formations and mechanical stability [1]. Similarly, frictional interactions play a significant role in the corrosion-driven failure of cementitious materials driven by precipitate growth [2, 3]. Capturing these interactions accurately within computational models is notoriously difficult due to the intricate interplay between contact forces and evolving geometries. In solid mechanics, contact problems are predominantly modeled using Lagrangian frameworks because the direct association between material points and discretization nodes facilitates straightforward tracking of displacements from the reference configuration, which is essential for implementing elastic constitutive laws. While the body-specific domains necessitate contact detection and resolution algorithms to couple different bodies [4], this close coupling makes the Lagrangian approach inherently well-suited for modeling the behavior of solid materials. Unfortunately, the Lagrangian description is not well suited for modeling evolving interfaces, such as in physical, chemical, or biological growth processes. A significant limitation is that any surface growth within a body requires a re-meshing procedure to accommodate changes in geometry. Nonetheless, such adaptations have been successfully implemented in certain cases (*e.g.*, [5]). Moreover, handling contact between evolving surfaces using Lagrangian finite elements is particularly costly due to the need for continuous detection and resolution of new contact regions. Consequently, existing Lagrangian approaches for modeling growth in

*Corresponding author

Email addresses: `florz@ethz.ch` (Flavio Lorez), `mpundir@ethz.ch` (Mohit Pundir)

constrained space simplify interfacial interactions by assuming perfect bonding and neglect complex phenomena like frictional sliding and adhesion, often relying on approximations such as Eshelby’s inclusion theory [6].

In contrast, Eulerian methods, where the computational mesh is fixed in space, provide a more straightforward approach to modeling evolving interfaces, being the natural choice for diffusion, transport or growth processes [7]. Although incorporating solid mechanics in Eulerian frameworks involves challenges such as surface tracking and obtaining the total deformation, these obstacles can be effectively addressed using established methodologies. Common approaches for tracking solid boundaries include the level-set method [8] and the phase-field technique [9, 10]. The computation of the deformation gradient, a key requirement for solid mechanics, can be achieved through the reference map technique, which enables precise calculation of total deformation within a fixed Eulerian mesh [11, 12, 13]. These advancements position the Eulerian approach as a promising option for unified modeling across a variety of physical processes.

In recent years, several studies, primarily in the context of fluid-structure interaction, have demonstrated that enforcing continuity of a single velocity field across the entire computational domain can effectively transmit pressure between contacting bodies [14, 12, 15, 16]. However, this approach inherently maintains a persistent gap between the bodies and restricts arbitrary sliding at the interface. To address these limitations, we recently introduced a new methodology for modeling frictionless contact within a fully Eulerian framework, where each body is represented separately using distinct motion functions and field variables [17]. By combining the reference map technique with the phase-field method to represent multiple bodies, we modeled contact using an implicit function defined in terms of the phase-field variables. This formulation enables arbitrary sliding between bodies and effectively handles large deformations and complex geometries without the need for explicit contact tracking. By separating interface interactions from the bulk motion of the bodies, we proposed a flexible framework that can be adapted to model more complex interfacial phenomena. Building on these foundations, we introduce a novel Eulerian formulation that systematically integrates frictional contact into the modeling framework. By employing separate sets of Eulerian field variables for each solid, similar to a Lagrangian multi-body representation, we preserve the independence of each body while enabling efficient coupling through contact constraints. This approach leverages the strengths of Eulerian methods such as simplified contact detection on a shared mesh and overcomes their traditional limitation of spurious bonding, thereby enabling accurate handling of frictional slip and stick behavior along interfaces.

The remainder of the paper is organized as follows. In Section 2, we present the Eulerian description of soft body motion and the incorporation of elasticity and the phase-field method for interface capturing. Section 3 revisits the frictionless contact formulation from [17] and details the frictional contact formulation using penalty-based body forces. The numerical implementation is discussed in Section 4. In Section 5, we provide numerical examples to validate and demonstrate the capabilities of the method. Finally, we conclude the paper with a discussion of advantages, challenges, and potential future work in Section 6.

2. Eulerian description of the motion of elastic bodies

In a classical Lagrangian description, the evolution of an elastic body \mathcal{B} is sufficiently described by the deformation map $\mathbf{x} = \chi(\mathbf{X}, t) : \mathbb{R}^D \times [0, T] \rightarrow \mathbb{R}^D$ (\mathbf{x} being the Eulerian coordinates, \mathbf{X} being the Lagrangian reference coordinates), that transforms the reference configuration \mathcal{B}_0 into the current configuration $\mathcal{B}(t)$ for all times t . The tangent of χ , the *deformation gradient* $\mathbf{F} = \partial\mathbf{x}/\partial\mathbf{X}$ describes the strain state.

2.1. Eulerian description of elasticity

To model elastic solids in an Eulerian frame, we employ the reference map technique [11, 18], which introduces the reference map $\mathbf{X} = \xi(\mathbf{x}, t) : \Omega \times [0, T] \rightarrow \mathbb{R}^D$, that maps the reference to the current configuration (see Fig. 1a). This approach allows for a consistent approximation of the deformation gradient, and consequently a way to model elastic solid laws in Eulerian frameworks. The deformation gradient is the inverse of the gradient of the reference map:

$$\frac{\partial\xi}{\partial\mathbf{x}} = \nabla\xi, \quad \mathbf{F}(\mathbf{x}, t) = \frac{\partial\mathbf{x}}{\partial\mathbf{X}} = (\nabla\xi(\mathbf{x}, t))^{-1}. \quad (1)$$

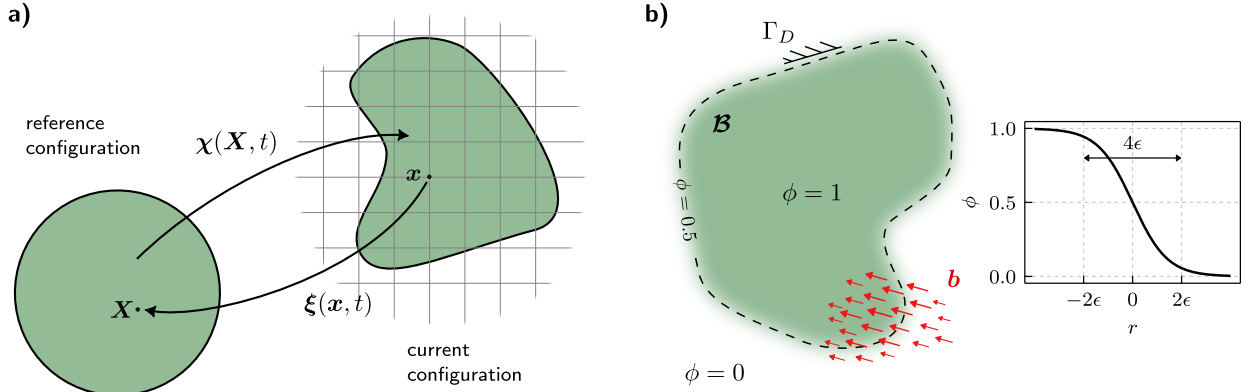


Figure 1: **(a)** An illustration of the reference map ξ . The reference map $\xi(\mathbf{x}, t)$ – being the inverse motion function $\chi(\mathbf{X}, t)$ – returns the reference location \mathbf{X} for any Eulerian coordinate \mathbf{x} . **(b)** Illustration of a body \mathcal{B} implicitly defined by a diffuse phase-field. The smooth transition of its boundary from $\phi = 1$ to $\phi = 0$ is shown in a 1D cut. The width of the transition zone is characterised by the parameter ϵ , where $\sim 90\%$ of the variation in ϕ lies within a width of 4ϵ . The possible presence of Dirichlet boundary conditions and force fields is indicated with Γ_D and \mathbf{b} .

Given the material velocity \mathbf{v} , any Eulerian field must be transported accordingly. For the reference position to remain unchanged from the perspective of a material point, the material time derivative $D\xi/Dt = 0$, provides the evolution law for the reference map:

$$\frac{D\xi}{Dt} = \frac{\partial \xi}{\partial t} + \mathbf{v} \cdot \nabla \xi = 0. \quad (2)$$

With access to the deformation gradient \mathbf{F} through the reference map ξ , any elastic constitutive relation can be formulated, such that:

$$\boldsymbol{\sigma} = f(\mathbf{F}), \quad (3)$$

where $\boldsymbol{\sigma}$ represents the stress tensor, and $f(\mathbf{F})$ describes the elastic material behavior.

The specific constitutive formulations utilized in this work are provided within the respective examples in Section 5.

2.2. Interface capturing with the phase-field method

We adopt the phase-field method to implicitly capture the domain of each body \mathcal{B}_i and its boundary $\partial\mathcal{B}_i$, by introducing auxiliary scalar fields $\phi_i(\mathbf{x}, t) \in [0, 1]$, where $\phi_i = 1$ and $\phi_i = 0$ define its solid and void phases, respectively (see Fig. 1b). The phase-field method is a diffuse interface approximation, characterized by a smooth transition over a finite but small width from solid to void phase that originates from the phase-field free energy functional [19, 9]:

$$\mathcal{E}_{\text{PF}}(\phi) = \int_{\Omega} \left(\frac{\epsilon^2}{2} (\nabla \phi)^2 + g(\phi) \right) d\Omega, \quad (4)$$

where ϵ^2 is the energy gradient coefficient, and $g(\phi) = \phi^2(1 - \phi)^2$ is a double-well potential with minima located at 0 and 1. The energetically favorable state of Eq. (4) yields the well-known tangent-hyperbolicus equilibrium profile normal to the interface, as shown in the inset of Fig. 1b,

$$\phi(r) = \frac{1}{2} \left[1 + \tanh \left(\frac{r}{\sqrt{2}\epsilon} \right) \right], \quad (5)$$

where r is the signed distance from the sharp interface.

In the absence of phase transformation and under pure mechanical deformation, the phase-field parameter ϕ_i should remain constant with respect to the reference coordinates \mathbf{X}_i . Equivalent to Eq. (2), the material

time derivative of ϕ_i yields the general evolution law

$$\frac{d\phi}{dt} = \frac{\partial\phi}{\partial t} + \mathbf{v} \cdot \nabla\phi = 0 . \quad (6)$$

While Eq. (6) theoretically preserves the original phase for all material points, it leads to a distortion of the diffuse interface, a phenomenon referred to as advective distortion [13, 9, 20, 21]. To counteract this, we consider the gradient flow towards minimizing the phase-field energy using an advective Cahn-Hilliard equation [22, 19, 23]:

$$\frac{d\phi}{dt} = \frac{\partial\phi}{\partial t} + \mathbf{v} \cdot \nabla\phi = \nabla \cdot (-\mathcal{M}\nabla q) , \quad q = \frac{\delta\mathcal{E}_{\text{PF}}}{\delta\phi} \quad (7)$$

where \mathcal{M} is a mobility coefficient controlling the magnitude of regularization. It must be highlighted that this regularization introduces an error in the conservation of the original body and must, therefore, be chosen carefully. To mitigate advective distortion while minimizing the impact of regularization, time-dependent mobility models have been proposed [20]. However, for simplicity, we adopt a constant mobility \mathcal{M} in this work.

We have chosen the fourth-order Cahn-Hilliard equation over the second-order Allen-Cahn equation because it is naturally volume conserving. Previous authors have presented concepts to make the Allen-Cahn equation volume conserving, *e.g.* [20, 21, 15, 23]. However, the mass correction term is usually non-local which complicates our implementation. As we will present in Section 4, we construct a single non-staggered variational minimization problem including the linear momentum balance, the phase-field and reference-map evolution equations. For similar reasons, we have refrained from making the phase-field a *constant* function of the reference map, as it has been done with level-set [12] or phase-field functions [13]. We require the phase-field to be part of the solution space because we later need its variation to find the optimal contact forces.

2.3. Conservation of linear momentum

The phase-fields ϕ track the interfaces while the reference maps ξ track the motion of material points. The combination of these two fields allows a definite description of the motion of deformable solid bodies in an Eulerian framework.

At time t , given some previous configuration \mathcal{B}_t with field variables ϕ_t and ξ_t , we aim to find a new configuration \mathcal{B}_{t+1} with field variables ϕ_{t+1} and ξ_{t+1} such that the linear momentum balance is satisfied:

$$\nabla \cdot (\phi\boldsymbol{\sigma}) - \mathbf{b} = \mathbf{0} , \quad (8)$$

where \mathbf{b} is an external force density. Contact forces are included as external forces, as will be described in Section 3.

Remark 1. *Reviewing Eq. (2), the velocity \mathbf{v} and reference map ξ can be strongly coupled. Therefore, we define the velocity field $\mathbf{v}(\xi)$ as an explicit function of the reference map ξ , effectively decreasing the number of unknowns:*

$$\mathbf{v}(\xi, t) = -(\nabla\xi)^{-1} \cdot \frac{\partial\xi}{\partial t} . \quad (9)$$

Because the weak form, which we will introduce in Section 4, has no terms containing $\partial\mathbf{v}/\partial x$, the velocity field \mathbf{v} is not required to be continuous. This allows for a discontinuous velocity field, obtained from the continuous space used for ξ .

3. Frictional contact formulation

In this section, we extend our previous work on a fully Eulerian model for frictionless contact [17] to frictional contact using penalty-based body forces for both normal and tangential traction components. We present the methodology for two body contact, however, any number of bodies can be included in a pairwise

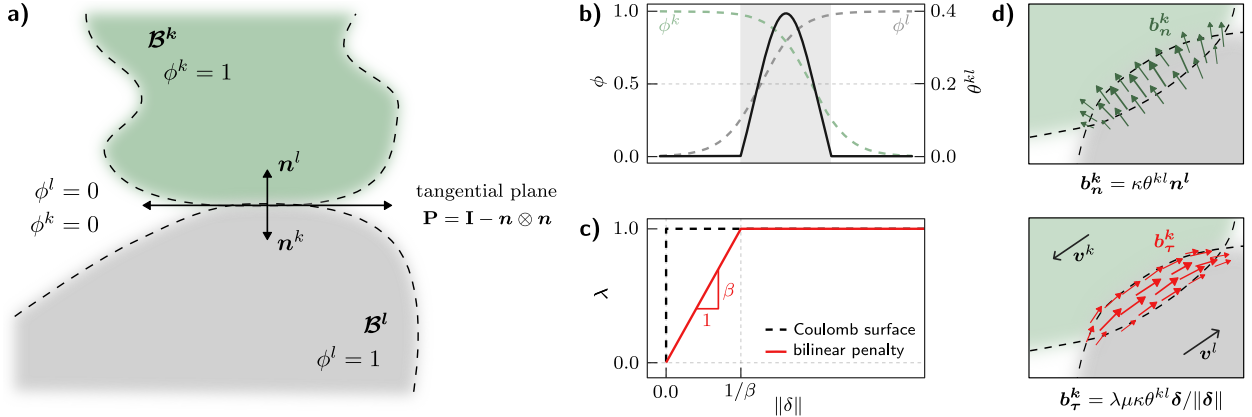


Figure 2: Schematic of the frictional contact formulation. **(a)** The two phase-fields ϕ_k and ϕ_l represent two elastic bodies in contact. We consider them to be in contact if their 0.5 iso-level sets intersect. The normals are used to define a projection matrix \mathbf{P} that is used to project the relative velocity $\bar{\mathbf{v}}_k$ onto the tangential plane. **(b)** 1D cut normal to the surfaces of the overlapping region. The intersection variable θ_{kl} is non-zero only in the immediate neighbourhood of regions where both phase-fields are > 0.5 . **(c)** The frictional penalty function, which is used to approximate the Coulomb friction law. **(d)** Illustration of the resulting normal and tangential force fields \mathbf{b}_n and \mathbf{b}_t .

manner. Consider two deformable bodies \mathcal{B}^k and \mathcal{B}^l which come into contact (see Fig. 2a). Following the framework presented in Section 2, each body is defined by its own set of field variables ϕ and ξ .

Unlike previous works, particularly in the context of fluid-structure interaction (FSI) [15, 16, 14], we employ a multi-velocity field approach. While a unified velocity field practically eliminates the need for additional contact forces due to the enforced continuity of the velocity field naturally preventing interpenetration, using separate velocity fields allows us to explicitly define the contact law. Furthermore, this approach facilitates sliding between bodies, which is generally not possible with a unified velocity field. To do so, we introduce a penalty body force field in Eq. (8) to minimize intersection of the phase-field variables ϕ^k , ϕ^l beyond their half-value $\phi = 0.5$, and hence, avoid inter-penetration of the bodies.

In the following, we use superscripts for the body index, subscripts n and τ to indicate normal and frictional components, and a further subscript t indicating the time step.

3.1. Normal contact formulation

To detect contact we define a scalar intersection variable for two bodies \mathcal{B}_k and \mathcal{B}_l as

$$\theta^{kl} := \left\langle \phi^k \cdot \phi^l - \frac{1}{4} \right\rangle^+, \quad (10)$$

where $\langle \cdot \rangle^+$ is the Macaulay bracket denoting the positive part of the argument. This intersection variable is illustrated for a 1D cut across the interface in normal direction in Fig. 2b. Due to the symmetry of two phase-fields, the intersection variable θ^{kl} is non-zero only in the immediate neighbourhood of regions where $\phi^k > 0.5$ and $\phi^l > 0.5$. In contrast to traditional contact formulations defined upon the gap function, the intersection variable is not directly proportional to the overlapping distance (it has an upper limit of $3/4$). Instead, the total reaction will be more sensitive to the volume of the contact zone.

Equation (10) defines a subset of the domain where contact forces are introduced. To construct a normal and tangential force field \mathbf{b}_n and \mathbf{b}_t , we make use of the available surface normals being the normalized gradients of the respective phase-field variables:

$$\mathbf{n}^k = \frac{\nabla \phi^k}{|\nabla \phi^k|}, \quad \mathbf{n}^l = \frac{\nabla \phi^l}{|\nabla \phi^l|}. \quad (11)$$

Introducing a normal penalty constant κ , the normal force field as proposed in [17] is defined as (Fig. 2d)

$$\mathbf{b}_n^k = \kappa \cdot \mathbf{n}^l \cdot \theta^{kl} . \quad (12)$$

3.2. Tangential traction and frictional contact

While our proposed method is agnostic to the choice of the friction law, for demonstration purposes, we focus on Coulomb friction in this work. Therefore we assume the tangential traction is proportional to the normal traction, with the proportionality constant being the friction coefficient μ . For a given slip rate δ and its magnitude $\|\delta\|$, the following relations apply:

$$\|\mathbf{b}_\tau\| \leq \mu \|\mathbf{b}_n\| \quad \text{and} \quad (13)$$

$$\|\delta\| \cdot (\mu \|\mathbf{b}_n\| - \|\mathbf{b}_\tau\|) = 0 \quad , \quad (14)$$

which define the admissible region in the $\|\delta\|$ - λ space as a Heaviside step function (see dashed black line in Fig. 2c).

We implement a penalty approach to enforce this condition, defining a tangential penalty constant β and a tangential penalty function $\lambda(\|\delta\|, \beta) : \mathbb{R}^+ \rightarrow [0, 1]$ for the magnitude of \mathbf{b}_t . The penalizing function λ should be a rapidly increasing continuous function of the slip rate, approximating the Heaviside step function:

$$\lambda(\|\delta\|, \beta) \sim H(\delta) := \begin{cases} 1 & \text{if } \|\delta\| > 0 \\ 0 & \text{if } \|\delta\| = 0 \end{cases} \quad (15)$$

In this work, we use a simple bilinear function for λ , ensuring that the penalty increases rapidly with a slope of $\partial\lambda/\partial\delta = \beta$. The function is displayed in Fig. 2b and reaches a value of 1 when $\|\delta\| \geq 1/\beta$, defined as:

$$\lambda(\|\delta\|, \beta) = \begin{cases} \beta\|\delta\| & \text{if } \|\delta\| < 1/\beta, \\ 1 & \text{otherwise,} \end{cases} \quad (16)$$

or equivalently,

$$\lambda(\|\delta\|, \beta) = \min(\beta\|\delta\|, 1) . \quad (17)$$

To implement a frictional force field, we leverage the known relative velocity between the two bodies that is naturally available due to the multi-velocity field formulation and the normals obtained from Eq. (11). The projection of the relative velocity $\bar{\mathbf{v}}_{kl} = \mathbf{v}_k - \mathbf{v}_l$ onto the tangential plane returns the slip rate δ :

$$\delta^{kl} = \mathbf{P} \cdot \bar{\mathbf{v}}^{kl} , \quad \mathbf{P} = \mathbf{I} - \mathbf{n}^l \otimes \mathbf{n}^l , \quad (18)$$

where \mathbf{P} is the projection operator onto the tangential plane, and \mathbf{I} is the identity tensor. Figures 2(a & d) provide an overview. The tangential force field acts opposite to the slip rate and is defined as:

$$\mathbf{b}_t^k(\phi^k, \phi^l, \mathbf{v}^k, \mathbf{v}^l, \kappa, \beta) = -\lambda(\|\delta^{kl}\|, \beta) \cdot \underbrace{\mu \cdot \kappa \cdot \theta^{kl}}_{\|\mathbf{b}_n^k\|} \cdot \frac{\delta^{kl}}{\|\delta^{kl}\|} . \quad (19)$$

Equation (19) expresses the tangential force as a direct function of the velocity fields \mathbf{v} and the phase-fields ϕ . The forces from Eq. (12) and Eq. (19) are incorporated into Eq. (8) to find the field variables ϕ and ξ for both bodies in a fully implicit way. For a multi-body system, contact force fields are included for all pairs of bodies in contact, and the total force field is the sum of all pair-wise contact forces. It is crucial to choose the penalty constants κ and β such that the contact forces are sufficiently large to minimize interpenetration in the normal direction and limit sliding for forces not on the Coulomb slip plane. The large gradients in the energy landscape inevitably lead to an ill-conditioned system, which is challenging to solve. To address this, we use an approach related to the interior point method [24] and the continuation method in topology optimization [25], which involves dynamically relaxing the constraint, progressively guiding the solution towards the feasible region. However, due to the non-convex nature of the energy landscape there

is a possibility that the method may settle in a suboptimal local minimum rather than the desired one. The details are presented in Section 4.2.

4. Numerical implementation

4.1. Discretization

For a system of N bodies, we construct a monolithic variational problem including the balance of linear momentum (Eq. (8)), the phase-field evolution (Eq. (7)), and the reference map evolution (Eq. (2)), for each body k . Any notion of time t refers to a pseudo time. The system is solved by the finite element method, where the weak form of the equations is discretized using linear shape functions.

Suppose \mathcal{S}_{f^k} and $\mathcal{V}_{\delta f^k}$ denote the space of trial and test functions for the functions $f^k \in \{\phi^k, \xi^k, q^k\}$ such that:

$$\mathcal{S}_{f^k} = \{f^k \in H^1(\Omega) \mid f^k = f_D^k \text{ on } \partial\Omega\} , \quad (20)$$

$$\mathcal{V}_{\delta f^k} = \{\delta f^k \in H^1(\Omega) \mid \delta f^k = 0 \text{ on } \partial\Omega\} . \quad (21)$$

The discrete variational form of the linear momentum balance equation at the next time $t + 1$ is given by:

$$\int_{\Omega} \phi_{t+1}^k \boldsymbol{\sigma}_{t+1}^k : \nabla \delta \xi^k \, d\Omega - \int_{\Omega} \mathbf{b}_{n,t+1}^k \cdot \delta \xi^k \, d\Omega - \int_{\Omega} \mathbf{b}_{\tau,t+1}^k \cdot \delta \xi^k \, d\Omega = 0 , \quad (22)$$

where $:$ denotes the double contraction of two second-order tensors (inner product). The penalty force densities \mathbf{b}_n^k and \mathbf{b}_{τ} are:

$$\mathbf{b}_{n,t+1}^k = - \sum_{l \in N} \kappa \cdot \mathbf{n}^l(\phi_{t+1}^l) \cdot \theta^{kl}(\phi_{t+1}^k, \phi_{t+1}^l) , \quad (23)$$

$$\mathbf{b}_{\tau,t+1}^k = - \sum_{l \in N} \lambda(\|\boldsymbol{\delta}^{kl}\|, \beta) \cdot \boldsymbol{\mu} \cdot \kappa \cdot \theta^{kl}(\phi_{t+1}^k, \phi_{t+1}^l) \cdot \frac{\boldsymbol{\delta}^{kl}}{\|\boldsymbol{\delta}^{kl}\|} . \quad (24)$$

Remark 2. We consider static equilibrium at $t + 1$. The tangential force density \mathbf{b}_t contains the slip rate $\boldsymbol{\delta}$ which is a function of the material velocities. For this, we use the intra-step velocity between $t \rightarrow t + 1$, therefore assuming a constant velocity in the timestep. This approach necessitates sufficiently small timesteps. A more accurate approximation of the velocity at $t + 1$ would be $(\mathbf{v}_{t+1/2} + \mathbf{v}_{t+3/2})/2$ which is unavailable in the currently employed scheme.

For temporal discretization of Eqs. (2) and (7), we use the Crank-Nicolson method. The semi-discrete form of the reference map evolution yields the velocity field $\mathbf{v}_{t+1/2} \in H^0(\Omega)$ as a function of the reference map $(\xi_{t+1}, \xi_t) \in (H^1(\Omega))^2$:

$$\mathbf{v}_{t+1/2}^k = -2 \left[\nabla \left(\frac{\xi_{t+1}^k + \xi_t^k}{2} \right) \right]^{-1} \frac{\xi_{t+1}^k - \xi_t^k}{\Delta t} . \quad (25)$$

To solve the fourth-order Cahn-Hilliard equation with first-order Finite Elements, we cast Eq. (7) into a system of two second-order equations, introducing the auxiliary variable $q = \delta \mathcal{E}_{\text{PF}} / \delta \phi$ [17]¹:

$$\int_{\Omega} \frac{\phi_{t+1} - \phi_t}{\Delta t} \delta \phi \, d\Omega + \int_{\Omega} \mathbf{v}_{t+1/2} \cdot \nabla \left(\frac{\phi_{t+1} + \phi_t}{2} \right) \delta \phi \, d\Omega + \mathcal{M} \int_{\Omega} (\nabla q \cdot \nabla \delta \phi) \, d\Omega = 0 , \quad (26)$$

$$\int_{\Omega} q \delta q \, d\Omega - \int_{\Omega} \epsilon^2 \nabla \left(\frac{\phi_{t+1} + \phi_t}{2} \right) \cdot \nabla \delta q \, d\Omega - \int_{\Omega} \left(\frac{g'(\phi_{t+1}) + g'(\phi_t)}{2} \right) \delta q \, d\Omega = 0 . \quad (27)$$

¹In our previous work [17], the auxiliary function was denoted with the symbol μ . Here, we changed it to not confuse it with the friction coefficient.

Then, the problem reads: Find the functions $(\xi_{t+1}^k, \phi_{t+1}^k, q_{t+1}^k) \in \mathcal{V} = (\mathcal{H}^1(\Omega))^3$ for every body such that Eqs. (22), (26) and (27) are satisfied. We implement the monolithic fully coupled system using FEniCS [26]. Schematically, for a single body, the system to solve looks as follows:

$$\underbrace{\begin{bmatrix} \mathbf{K}_\xi & \mathbf{K}_{\xi\phi} & 0 \\ & \mathbf{K}_\phi & \mathbf{K}_{\phi q} \\ & & \mathbf{K}_q \end{bmatrix}}_{\mathbf{K}^{(k)}} \cdot \underbrace{\begin{bmatrix} \xi \\ \phi \\ q \end{bmatrix}}_{\mathbf{u}^{(k)}} - \underbrace{\begin{bmatrix} \mathbf{b} \\ 0 \\ 0 \end{bmatrix}}_{\mathbf{f}^{(k)}} = \mathbf{0} \quad (28)$$

Considering multiple bodies, the system is constructed as follows:

$$\begin{bmatrix} [\mathbf{K}^{(k)}] & 0 \\ & [\mathbf{K}^{(l)}] \end{bmatrix} \cdot \begin{bmatrix} \mathbf{u}^{(k)} \\ \mathbf{u}^{(l)} \end{bmatrix} - \begin{bmatrix} \mathbf{f}^{(k)} \\ \mathbf{f}^{(l)} \end{bmatrix} = \mathbf{0} \quad (29)$$

4.2. Solver details

The resulting non-linear system is solved using PETSc's *SNES* solver, employing the Newton method with line search, *MUMPS* for the linearized subproblems, and *AMG* pre-conditioning [27].

To resolve the frictional inequality to high accuracy, in particular to retrieve the slip-stick differentiation, relatively large penalty coefficients β are required. However, for large penalty coefficients β , the frictional penalty forces in the contact formulation lead to a highly ill-conditioned system, which is challenging to solve. Furthermore, the problem is magnified by the reduced admissible solution space constrained by the Lorentz cone.

Therefore, to reliably obtain a solution, we decompose the problem into two subproblems: First, we address the stick problem, where the frictional force is linearly proportional to the slip rate. Second, we progressively allow slip to return to the Coulomb slip surface, which is effectively equivalent to a return mapping algorithm.

Algorithm 1: Continuation method and return mapping

Input: Non-linear minimization problem \mathcal{P} , starting point \mathbf{u}_0 , target penalty parameter β_t , increment factor γ_β^+ , reduction factor γ_β^- , slip mixing increment $\Delta\alpha$.

Output: Solution \mathbf{u}

$\beta \leftarrow \beta_t$

$\alpha \leftarrow 0$

$\mathbf{u} \leftarrow \mathbf{u}_0$

while do

 Backup \mathbf{u} : $\mathbf{u}_* \leftarrow \mathbf{u}$

if Minimize \mathcal{P} : $\mathbf{u} \leftarrow \min \mathcal{P}(\mathbf{u}, \beta)$ **then**

if $\beta \geq \beta_t$ **then**

break

 Increase penalty $\beta \leftarrow \gamma_\beta^+ \beta$

else

 Revert $\mathbf{u} \leftarrow \mathbf{u}_*$

 Reduce penalty $\beta \leftarrow \gamma_\beta^- \beta$

while $\alpha < 1$ **do**

 Minimize \mathcal{P} : $\mathbf{u} \leftarrow \min \mathcal{P}(\mathbf{u}, \alpha)$

 Increase slip mixing $\alpha \leftarrow \alpha + \Delta\alpha$

return \mathbf{u}

4.2.1. Continuation method

To solve the stick-only problem, we employ the continuation method, which incrementally increases the constraints to guide the solution toward the feasible region, if necessary. This approach helps mitigate ill-conditioning by avoiding large, abrupt changes in the solution space. The continuation method can be viewed as a generalization of the penalty method, where the penalty parameter is dynamically adjusted to approach the solution of the original problem [25]. It can also be seen as a simplification of the augmented Lagrangian method [28], and shares principles with the interior point method (IPM).

However, due to the non-convex nature of the frictional contact problem, the continuation method may not always guarantee a unique solution. While the method is generally effective at finding the global optimum, our primary interest lies in identifying the local minimum, particularly by leveraging the variation of the previous solution. Therefore, caution is warranted when applying the continuation method in this context, as there is a risk of converging to an unintended local minimum. To reduce this risk, we start with the target penalty parameter β_t and decrease it only if the solver fails to converge. The procedure is outlined in Algorithm 1.

4.2.2. Return mapping

After solving the stick problem, we introduce slip by incrementally increasing the slip mixing parameter α from 0 to 1. This scalar parameter linearly interpolates between the stick and slip solutions, allowing for a smooth transition between these two states:

$$\lambda = (1 - \alpha)\lambda_{\text{stick}} + \alpha\lambda_{\text{Coulomb}} , \quad (30)$$

$$\lambda_{\text{stick}}(\delta, \beta) = \beta\delta , \quad \lambda_{\text{Coulomb}}(\delta, \beta) = \min(\beta\delta, 1) . \quad (31)$$

The return mapping process is demonstrated in Section 5.1.2, and the method is outlined in Algorithm 1. We acknowledge that the current approach may not be optimal, and potential improvements are identified as areas for future work.

5. Examples

In this section, we present three numerical examples to validate and showcase the proposed methodology. Throughout the examples, we use dimensionless units for space and time. We start by validating the proposed methodology for the Cattaneo-Mindlin problem, a classical benchmark problem for frictional contact for which an analytical solution is available [29, 30]. We first demonstrate that our method yields the correct traction profile, and investigate the return mapping process to illustrate the internal solution process. We also show the path dependency by performing a full cycle of forward and backward sliding, and show that a reasonable hysteresis loop is obtained when sliding the bodies back and forth. Next, we simulate the ironing problem to show large sliding [31, 32, 33]. In the last example, we analyze a system with two deformable solids and multiple contact patches. For all shown examples, we use dimensionless units.

5.1. Cattaneo-Mindlin problem

5.1.1. Tangential traction profile

The Cattaneo-Mindlin problem is a classical benchmark problem for frictional contact [29, 30]. The problem consists of two linear elastic cylinders in contact, pushed together and then sheared. The setup is shown in the inset of Fig. 3a. Equivalent to the Hertzian solution, the analytical solution for the tangential traction profile, given the total normal and tangential reaction force, is known. We use this problem to test the proposed methodology for frictional contact with partial slip, specifically focusing on whether the differentiation between sliding and sticking regions is correctly captured. The two cylinders are modeled as linear elastic, *i.e.*

$$\boldsymbol{\sigma} = \lambda \text{tr}(\boldsymbol{\varepsilon})\mathbf{I} + 2\mu\boldsymbol{\varepsilon} , \quad \boldsymbol{\varepsilon} = \frac{1}{2}(\mathbf{F} + \mathbf{F}^T) - \mathbf{I} . \quad (32)$$

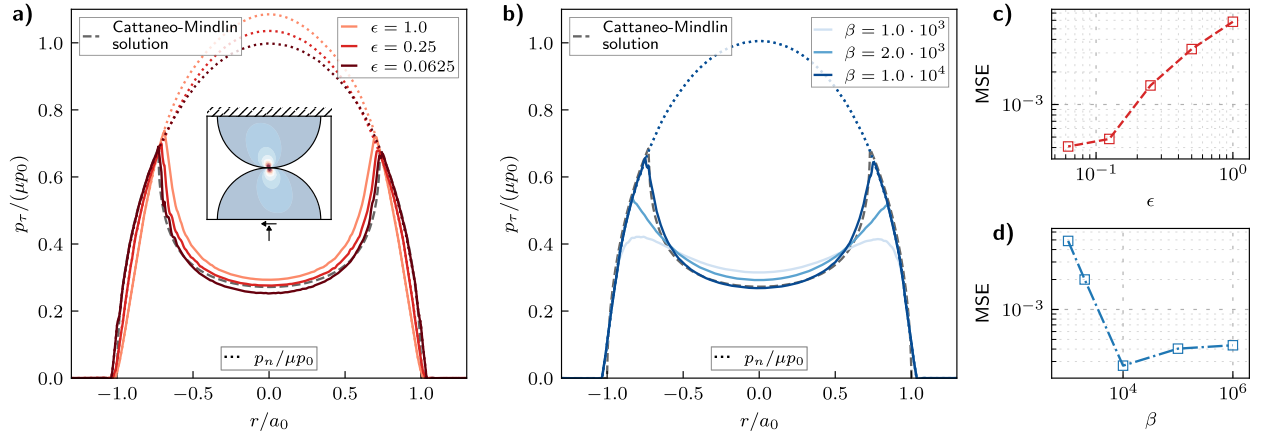


Figure 3: Analysis of the tangential traction profile for different values of diffuse interface width ϵ and frictional penalty coefficients β in the Cattaneo-Mindlin problem. For all displayed cases, the normal penalty is $\kappa = 200$, and the mobility parameter is $\mathcal{M} = 10^{-6}$. **(a)** Normalized traction profile for varying ϵ . The analytical solution is shown as the dashed black line. The dotted lines are the normal traction (μp_n). **(b)** Normalized traction profile for varying β (for $\epsilon = 0.125$). **(c, d)** Mean squared error (MSE) between the resulting traction profile and the analytical solution for increasing ϵ and β , respectively.

They have a radius of $R_0 = R_1 = 10$, Young's modulus $E_0 = E_1 = 0.2$, and Poisson's ratio $\nu_0 = \nu_1 = 0.2$. The friction coefficient is $\mu = 0.5$. We clamp the top cylinder at its top boundary and apply to the bottom cylinder first, a vertical displacement $\bar{u}_y = 0.03$ and then a horizontal displacement of $\bar{u}_x = 0.01$.

The analytical solution of the traction profile is characterized by the effective young's modulus E^* , the contact zone width a , the stick-slip transition width c , the normal and tangential reaction forces P_n and P_τ , and the friction coefficient μ :

$$E^* = \left(\frac{1 - \nu_0^2}{E_0} + \frac{1 - \nu_1^2}{E_1} \right)^{-1}, \quad R = \left(\frac{1}{R_0} + \frac{1}{R_1} \right)^{-1}, \quad a = \left(\frac{4P_n R}{\pi E^*} \right)^{1/2}, \quad c = a \left(1 - \frac{P_\tau}{\mu P_n} \right)^{1/2} \quad (33)$$

Then, the analytical solution for the normal and tangential traction profiles were found to be:

$$p_n(r) = \frac{2P_n}{\pi a^2} \sqrt{a^2 - r^2}, \quad (34)$$

$$p_\tau(r) = \frac{2\mu P_n}{\pi a^2} \left(\sqrt{a^2 - r^2} - H(c^2 - r^2) \sqrt{c^2 - r^2} \right). \quad (35)$$

Figure 3 demonstrates the strong agreement between our numerical experiments and the analytical solution. To achieve this, we define the traction as the integrated force density perpendicular to the surface, denoted as $p_\tau = \int_n \mathbf{b}_\tau \, dn$, and the reaction force as the volume integral $P_\tau = \int_\Omega \mathbf{b}_\tau \, d\Omega$. We normalize the traction profile using the maximum Hertzian traction at $r = 0$. For a review of the normal traction profile, the reader is referred to [17].

In Fig. 3a, we display the traction for various values of the diffuse interface width ϵ , with the analytical solution represented by the dashed black line. The normal traction (scaled with μ) is depicted as the dotted line. As ϵ decreases, the numerical solution approaches the analytical solution. It is important to note that the normalization obscures the fact that the absolute traction is lower for large ϵ than the smaller ϵ due to the softer implied contact stiffness (for equal κ). In Fig. 3b, we show the traction for varying frictional penalty coefficients β for a fixed $\epsilon = 0.125$. It is evident that the solution is converging for sufficiently large β . The mean squared error (MSE) between the numerical and analytical solutions is shown in Fig. 3(c, d). The error does not decrease further for $\beta > 10^4$ due to limitations from the discretization. Further h -refinement would be required to reduce the error further. Overall, the results demonstrate that the proposed methodology is capable to accurately capture the tangential traction profile for the Cattaneo-Mindlin problem.

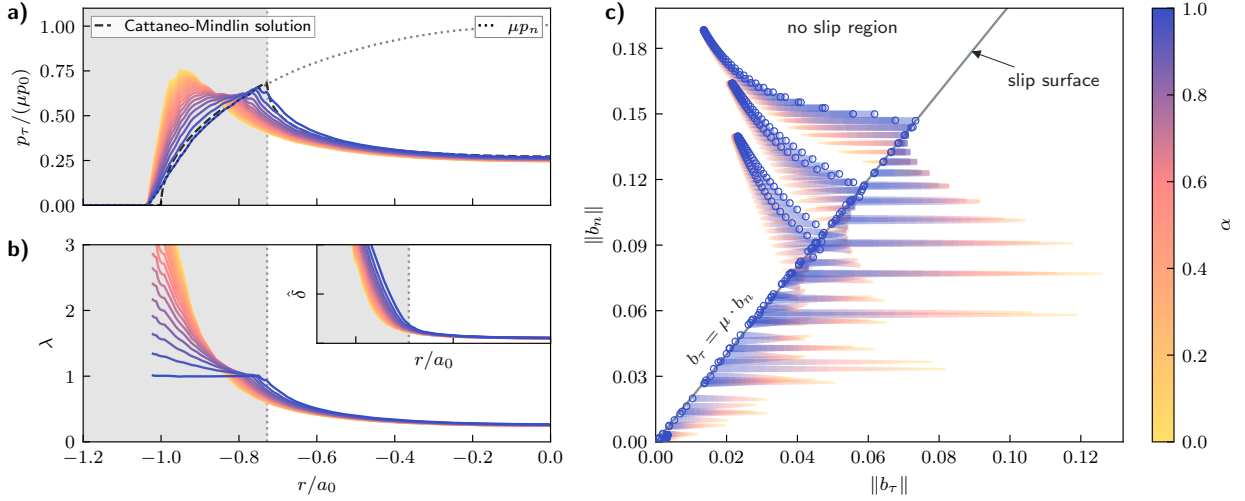


Figure 4: Illustration of the implicit return mapping on the example of a single Cattaneo-Mindlin simulation with $\epsilon = 0.125$ and $\beta = 10^4$. **(a)** Intra-step evolution of the traction profile with the implicit return mapping. Starting from a strictly sticking interface ($\alpha = 0$) to a partially sliding interface ($\alpha = 1$). The dashed black line is the analytical solution. **(b)** The local effective slip rate $\hat{\delta}$ for every position in the contact patch. **(c)** The local absolute contact force densities b_n and b_τ for every node in the contact zone, from $\alpha = 0$ to $\alpha = 1$. Every trace represents one node, and the round markers indicate the final state. For nodes where the tangential force initially exceeds the valid value of μb_n , the tangential component is effectively reduced to the slip surface.

5.1.2. Return mapping illustration

Figure 4 illustrates the implicit return mapping for a single Cattaneo-Mindlin simulation with $\epsilon = 0.125$ and $\beta = 10^4$. The figure shows the intra-step evolution from $\alpha = 0$ (yellow) to $\alpha = 1$ (blue) of the traction profile (Fig. 4a), the value of λ , and the local slip rate δ in the contact zone (Fig. 4b), and the local absolute force densities b_n and b_τ for every node in the contact zone (Fig. 4c). The figure demonstrates the correct differentiation between sticking and sliding regions, as well as the correct enforcement of the frictional law. In Fig. 4c, for nodes where the tangential force initially exceeds the admissible maximum of μb_n , the tangential component is effectively reduced to the slip surface (Lorentz cone).

In the left part of Fig. 4, the tractions, being the integrated force densities across the contact patch, and the frictional function $\lambda(r)$ are computed as:

$$p_n(r) = \int_y b_n(r, y) dy, \quad p_\tau(r) = \int_y b_\tau(r, y) dy, \quad \lambda(r) = \frac{p_\tau(r)}{\mu p_n(r)}, \quad (36)$$

and the effective slip rate $\hat{\delta}$ according to Eq. (37). For $\alpha = 0$, considered to be an artificial state of full stick, the tangential traction is maximal at the edge of the contact area. When the Coulomb friction law is consecutively mixed in by increasing α , the tangential traction profile transitions to the analytical solution.

The right part of Fig. 4 illustrates the local force densities b_n and b_τ for every node in the contact zone. The three distinct clusters of nodes represent three layers of nodes in normal direction inside the volumetric contact patch. While for $\alpha = 0$, the points span the entire space, for $\alpha = 1$, all points are inside the admissible friction cone or lay exactly on the slip surface $b_n = \mu b_\tau$. Further we observe that most points shift in horizontal direction, meaning that the return mapping process works mainly by implicitly altering the tangential force density by altering the horizontal component of displacement, while maintaining a constant normal pressure.

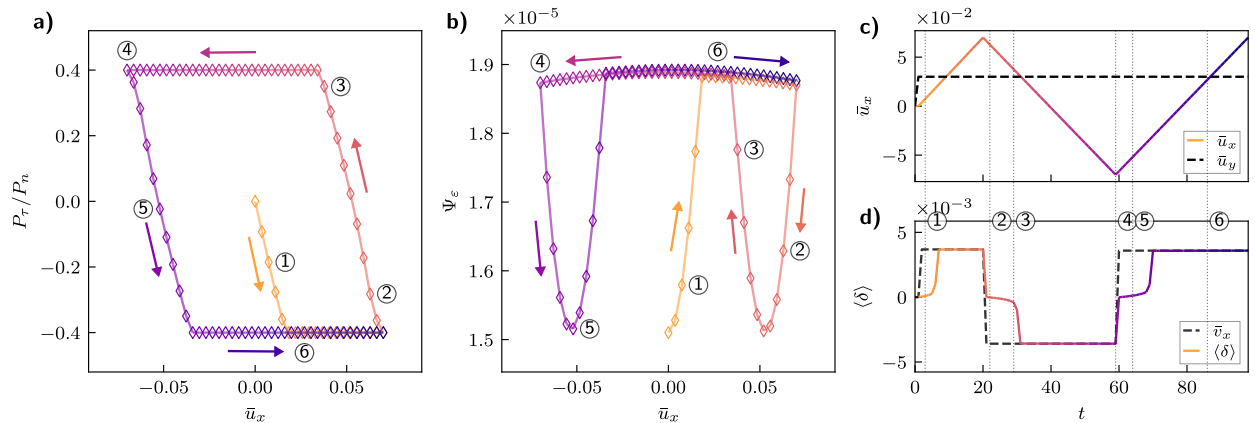


Figure 5: Hysteresis loop for the Cattaneo-Mindlin problem. The figure shows the tangential reaction force P_τ for the forward and backward loading paths. The hysteresis loop is a result of the path-dependent energy dissipation in the frictional contact problem. ① Initial tangential loading; partial slip. ② Point of reversal; stick and unloading. ③ On the brink of slipping. ④ Full slip. ⑤ Neutral total friction force; partial slip. ⑥ Full slip. (a) Tangential reaction force in time. The x -axis shows the applied position at the bottom of the bottom cylinder, while the y -axis shows the normalized reaction force P_τ/P_n . (b) Integrated strain energy. (c) Applied motion at the bottom edge of the bottom cylinder. First, a vertical velocity is applied, followed by a full cycle of forward and backward horizontal motion. (d) Averaged slip rate at the contact interface, in comparison to the applied velocity of the bottom edge of the bottom cylinder.

5.1.3. Hysteresis loop

To illustrate path-dependent energy dissipation in the frictional contact problem, we consider the same setup as in Section 5.1.1 and conduct a complete cycle of forward and backward shearing motion. The used parameters are $E = 0.2$, $\nu = 0.2$, $\mu = 0.4$, $\epsilon = 0.125$, $\mathcal{M} = 10^{-8}$, $\kappa = 300$, and $\beta = 4 \cdot 10^4$. We prescribe the motion of the bottom half cylinder, which is depicted in Fig. 5c. Initially, the bottom cylinder is moved vertically by $\bar{u}_y = 0.03$, followed by a horizontal motion within $\bar{u}_x \in [-0.07, 0.07]$. Throughout Fig. 5, we indicate six characteristic stages with annotations 1 to 6.

Figure 5(a,b) show the hysteresis loop for the relative tangential reaction force P_τ/P_n and the strain energy Ψ_ϵ respectively. The hysteresis loop reveals an expected path-dependent energy dissipation, where the forward and backward loading paths are clearly distinguishable. In addition, Fig. 5d shows the average slip rate $\langle \delta \rangle$ in the contact patch in comparison to the applied bottom boundary velocity \bar{v}_x . To compute the average slip rate across the contact patch, we first define an effective slip rate across its thickness using a weighted average of the slip rate $\delta(r, y)$ and the tangential force density $b_\tau(r, y)$;

$$\hat{\delta}(r) = \frac{\int_y \delta(r, y) \cdot b_\tau(r, y) dy}{\int_y b_\tau(r, y) dy}, \quad (37)$$

and then average the effective slip rate across the width of the contact patch:

$$\langle \delta \rangle = \frac{\int_r \hat{\delta}(r) dr}{\int_r 1 dr}. \quad (38)$$

The discontinuities in $\langle \delta \rangle$ align with the transition points in the applied velocity, showing characteristic jumps near stage 2 and 4 when the motion is reversed. Upon the reversal of the external motion, $\langle \delta \rangle$ stays close to 0, meaning a sticking interface; then it grows in magnitude until the full contact patch is in a sliding state and the average slip rate equals the externally applied velocity. This behavior highlights a stick-slip phenomenon at the interface, where the contact patch transitions from full stick to full slip.

5.2. Ironing problem

The ironing problem is a benchmark for testing large sliding in contact formulations [31, 32, 33]. In this setup, a rigid cylindrical die with a radius of $R = 0.5$ is pressed into a deformable box with dimensions 3×1 , which is fixed at the bottom (see Fig. 6). The box material is modeled as a Neo-Hookean hyperelastic material law with Young's modulus $E = 1.0$ and Poisson's ratio $\nu = 0.3$. Its strain energy density is given by:

$$W = \frac{\mu}{2} (\text{tr}(\mathbf{C}) - d) - \mu \ln J + \frac{\lambda}{2} (\ln J)^2, \quad (39)$$

where μ and λ are the Lamé parameters, d is the dimension of the space, $J = \det(\mathbf{F})$, and $\mathbf{C} = \mathbf{F}^T \mathbf{F}$ is the right Cauchy-Green deformation tensor. The Cauchy stress is given by:

$$\boldsymbol{\sigma} = \frac{\mu}{J} (\mathbf{F}\mathbf{F}^T - \mathbf{I}) + \frac{\lambda}{J} (\ln J) \mathbf{I}. \quad (40)$$

The phase-field model parameters are set to $\epsilon = 0.02$ and $\mathcal{M} = 10^{-6}$. The contact is modeled as frictional, with a coefficient of friction $\mu = 0.3$, while the penalty parameters are set to $\kappa = 10^3$ and $\beta = 10^3$. The die follows a prescribed motion as depicted in Fig. 6c. Initially, a uniform downward displacement of $\bar{u}_y = -0.075$ is applied over 10 time steps, followed by a horizontal displacement of $\bar{u}_x = 2.0$ over the subsequent 100 time steps.

We employ the proposed methodology to solve the problem, demonstrating its ability to handle arbitrarily large sliding. Figure 6a presents the problem setup along with the von Mises stress distribution. Two instances are shown: first (left side), after completing the vertical displacement (marked as ①), and later, towards the end of the simulation (marked as ②). As expected, the sliding generates horizontal forces, resulting in a characteristic skewed stress profile.

In Fig. 6b, we plot the reaction forces P_τ and P_n over the course of the simulation. Zoomed-in views are provided in Fig. 6d and (e) to enhance clarity along the y -axis. Initially, we observe an approximately linear increase in the normal reaction up to ①, accompanied by a small tangential reaction due to the asymmetric box loading. Once the die begins horizontal motion, the frictional reaction quickly saturates at $P_\tau = \mu P_n$. Shortly after ①, a slight increase in the reaction force is observed, attributed to rotational effects induced by the frictional force, which cause greater compression in the system.

While comparable studies employing Lagrangian approaches report small oscillations in reaction forces due to sliding across element boundaries, along with strategies to mitigate these effects [33], the reactions in our results are perfectly smooth. This is no surprise, since the fixed mesh inherent to an Eulerian approach eliminates the presumed source of these oscillations. Compared to the results in [33], the reaction forces in our study are approximately 10% lower in magnitude. This discrepancy likely arises from the diffuse interface approximation and the deformation of the softer transition zone ($\phi = 0.5 \rightarrow 1$) at the interface, which acts as a deformation buffer. The effect is further pronounced due to the displacement-controlled loading in this setup, as the reaction forces are effectively reduced by the deformation of the *softer* interface.

Lastly, we note that no convergence issues were encountered with the parameters used in this simulation.

5.3. Multi-patch frictional contact

We use the final example to demonstrate the applicability of the proposed methodology to systems with multiple contact patches between deformable bodies (Fig. 7a). The top body features three sinusoidal asperities of varying magnitudes that interact with the flat surface of the bottom body. Initially, the top body is displaced downward by a total vertical displacement of 0.03, compressing both bodies. Subsequently, it is moved laterally to the right with a constant boundary velocity of $\bar{v}_x = 2.5 \cdot 10^{-3}$, generating frictional forces at the interface.

All simulation units are dimensionless. The material is modeled as Neo-Hookean elastic (see Eqs. (39) and (40)) with $E = 0.6$ and $\nu = 0.3$. The phase-field parameters are $\mathcal{M} = 5 \cdot 10^{-7}$ and $\epsilon = 0.01$, while the contact parameters are $\kappa = 5 \cdot 10^3$, $\beta = 1 \cdot 10^3$, and $\mu = 0.4$.

The system setup can be inferred from Fig. 7. The system of equations from Eqs. (22), (26) and (27) is solved subject to the following boundary conditions:

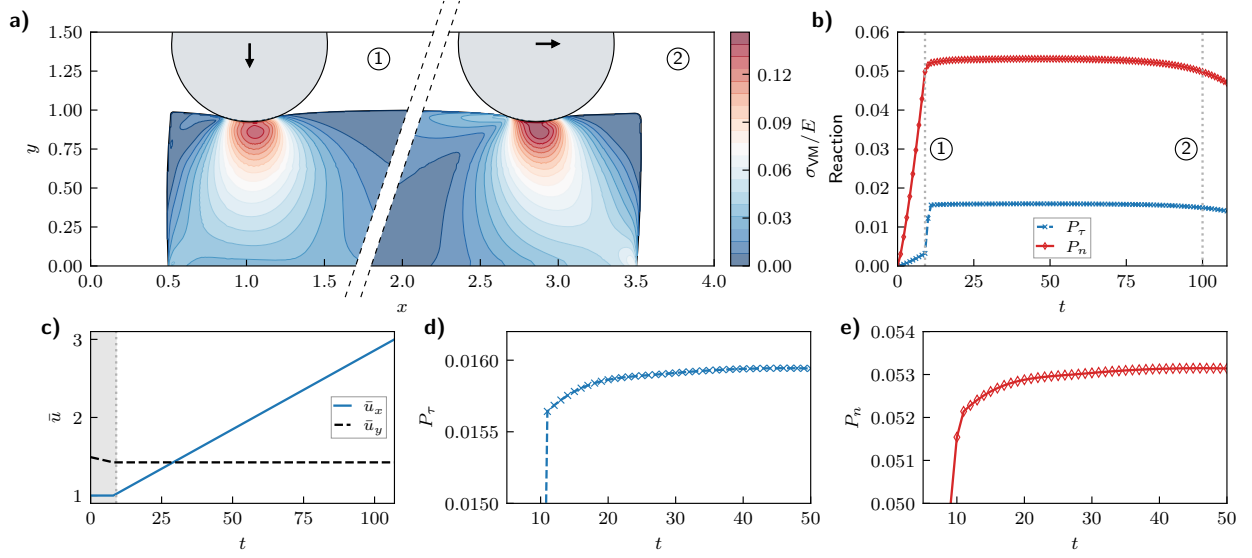


Figure 6: Ironing problem. (a) Problem setup and von Mises stress intensity for two time instances: ① shows the state when the die has reached its final vertical position, and ② depicts the die at a later time during horizontal sliding. (b) Reaction forces P_τ (tangential) and P_n (normal) over the course of the simulation. (c) Prescribed motion of the rigid die. First a vertical displacement of $\bar{u}_y = -0.075$ is applied in 10 steps, followed by a horizontal displacement of $\bar{u}_x = 2.0$ in a further 100 steps. (d, e) Zoomed-in view of the reaction forces P_τ and P_n .

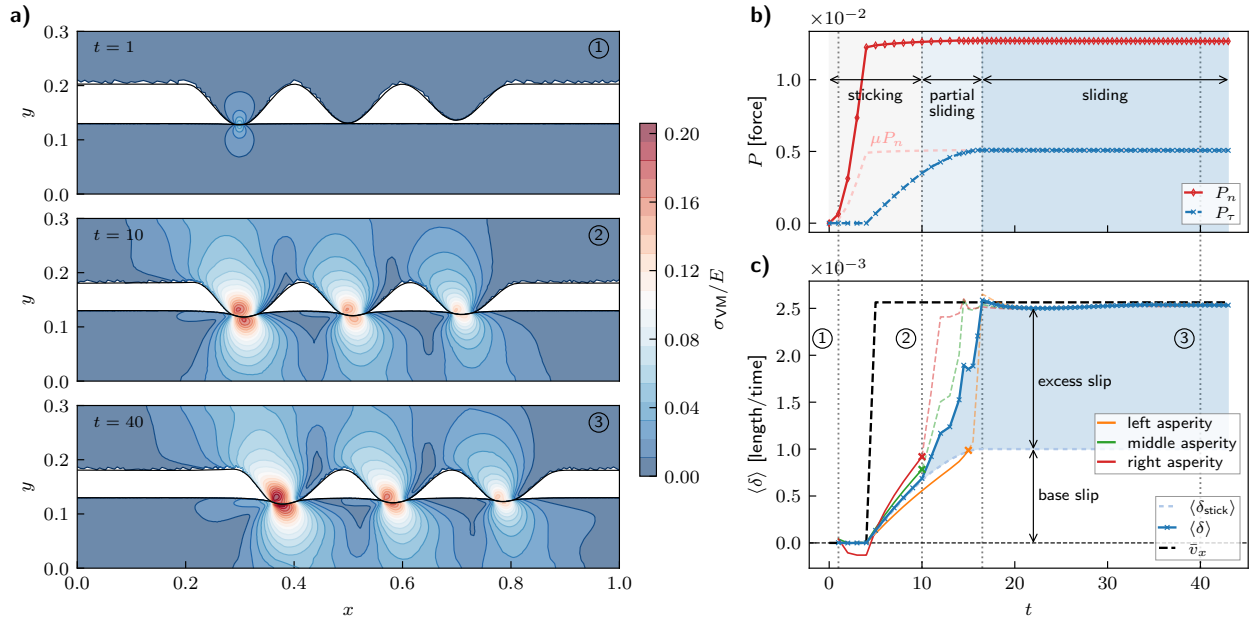


Figure 7: Frictional contact between a body with sinusoidal asperities and a flat plane. (a) Problem setup and von Mises stress intensity for three instances in time. (b) Total normal and tangential reaction forces over time. (c) Slip rates as a function of time, averaged over the total contact area (blue) and over the contact area of individual asperities (orange, green, red). The base slip rate is the slip required to reach the sliding surface of Coulomb's law and thus, the erroneous sliding of a sticking interface introduced by the taken penalty approach. For each asperity, the cross marks the moment, when the recorded slip rate exceeds the base slip rate, marking the onset of sliding. The dashed black line shows the prescribed velocity of the top body.

- For the upper body, the reference map ξ is prescribed on the upper boundary as $\xi_{t+1} = \xi_t - \bar{\mathbf{v}}\Delta t$, corresponding to the imposed boundary motion $\bar{\mathbf{v}}$. On the lateral sides, only the x -component of ξ is prescribed.
- For the bottom body, the reference map ξ is fixed at its initial value, $\xi_{t+1} = \xi_t$ at all edges.

Figure 7a shows the von Mises stress distribution inside the body – where $\phi > 0.5$ – at three time instances. Due to the asymmetry of the asperities, the stress distribution varies among them. Furthermore, friction causes a skewed stress distribution.

Figure 7b illustrates the total tangential and normal reaction forces over time. The tangential force increases continuously as the top body moves right. Around $t = 17$, the tangential force plateaus, indicating that the interface is in full sliding.

The slip rate over time is shown in Fig. 7c, where the average slip rate across the contact area (blue) and individual asperities (orange, green, red) are plotted. Due to the penalty approach used to enforce Coulomb’s law, a base slip exists even for a *sticking* interface. This base slip corresponds to the minimal required slip rate to achieve the observed frictional force and is determined by the ratio of the average tangential force density p_τ to the normal force density p_n , scaled inversely by $\beta\mu$:

$$p_\tau = \underbrace{\beta\delta}_{\lambda} (\mu p_n) \longrightarrow \langle \delta_{\text{stick}} \rangle = \frac{\langle p_\tau \rangle}{\beta\mu \langle p_n \rangle} \quad , \quad (41)$$

where $\langle \cdot \rangle$ denotes an average over the contact area according to Eqs. (37) and (38). We consider that sliding begins when the recorded slip exceeds this base slip. The onset of sliding of the individual asperities is marked by the crosses in Fig. 7c.

Sliding initiates at $t = 10$ (time instance 2) when the middle and right asperities begin to slide, while the leftmost and most loaded asperity remains sticking. After this, the system is in a state of partial slip until $t \approx 17$, at which point the total slip rate matches the top body’s velocity (dashed black line), indicating full sliding. The third time instance shows the interface in a state of full sliding. We note that the proposed methodology is capable of effectively capturing interfacial forces at multiple contact patches.

6. Discussion

In this work, we introduced a novel Eulerian phase-field framework to model frictional contact between deformable bodies. To the best of our knowledge, this is the first fully functional method that incorporates frictional contact within a Eulerian phase-field context. By leveraging the reference map technique in combination with the phase-field method, we developed an approach that captures large deformations, complex contact interactions, and frictional effects within a Eulerian setting.

A major benefit of the original Eulerian approach [17] has been its simplicity. Contact interactions are implicitly captured through the overlap of diffuse phase-fields, while penalty-based body forces enforce contact constraints. Extending this method to handle frictional contact maintains this simplicity, utilizing the available field variables on the Eulerian mesh to construct frictional penalty forces. Lagrangian contact formulations often rely on node-to-node or node-to-segment contact definitions, which can restrict sliding to small incremental changes and induce subtle oscillations originating from the discretization of the surfaces in contact [33]. The implicit representation of bodies through phase-field variables allows for sliding without restrictions, enabling the simulation of arbitrarily large sliding motions and the handling of complex shapes. Furthermore, the suggested methodology retains all the inherent advantages of an Eulerian formulation, which is particularly suited for problems involving large deformations, multiphysical problems, where contact interactions are coupled with other physical or chemical phenomena, for which the Eulerian description is more natural. For example, Eulerian formulations have been prominently used to model fluid-structure interactions [34, 18, 35, 14, 36, 21], to model growth processes [37, 38, 39] or problems related to topological changes such as merging and separation of bodies [40, 41].

While we have demonstrated the method using Coulomb friction, there is nothing conceptually limiting the implementation of more refined friction laws by adapting the frictional penalty force function Eq. (19), such as rate-and-state friction models [42, 43]. As illustrated in Fig. 4, the method respects the transition from sticking to sliding, accurately representing history dependence and energy dissipation associated with frictional interactions, and the simulations exhibit oscillation-free frictional responses during sliding.

However, several challenges remain or were discovered during the construction of this paper. Whereas the proposed method could be used to solve the Coulomb friction problem by a simple minimization using the Newton method, accurately capturing the stick-slip differentiation requires a large frictional penalty coefficient β , which leads to an ill-conditioned system and consequently convergence difficulties for any numerical solver. We addressed this by employing an incremental penalty approach, gradually increasing the penalty parameters to guide the solution toward the feasible region. Such an approach is strongly related to the interior point method (IPM) and Barrier methods. The name continuation method is borrowed from topology optimization, where it is used to find the global minimum of a non-convex problem by gradually increasing the penalty parameter [25]. In general, all these methods have in common to find a global minimum of a non-convex minimization problem, which does not include friction. To mitigate the risk of deviating from the local energy well, we propose a two-way penalty continuation. By starting with the target penalty, gradually decreasing it until the system is well-conditioned enough to find the solution, and finally increasing the penalty to the target again, we restrict the nature of such an approach to land at the global minimum. However, while this mitigates some of the numerical challenges, it undoubtedly introduces additional complexity.

Another, obvious, challenge arises from the diffuse representation by incorporating the phase-field method. The size of the transition zone, controlled by the phase-field energy gradient parameter ϵ , has a significant impact on the frictional behavior. A large transition zone softens the contact and leads to a larger spread of the contact forces over a wider area, which may not be desirable in applications requiring high precision. On the other hand, a small transition zone can lead to a high sensitivity to mesh resolution and may introduce numerical artifacts [17]. Furthermore, the nodes of a contact patch become volumetrically distributed rather than being confined to a single contact line. This means that multiple layers of nodes within the contact patch contribute to the frictional response. For the frictional force, this means that, while the forces integrated over the width of the contact patch are consistent with the analytical Cattaneo-Mindlin solution (see Fig. 3), the force density is not necessarily constant across the contact patch. This may introduce unphysical shearing of the diffuse interface.

Looking forward, this work opens several avenues for future research. Applying the method to model multiphysical systems involving contact and friction could provide valuable insights into phenomena such as biofilm growth, where friction plays a significant role in how the film grows [1]. We believe our proposed framework can be helpful in understanding how growth processes are affected by frictional interaction with the environment, which could provide valuable insight in biology and materials science.

7. Conclusion

In this paper, we extended the novel Eulerian framework incorporating a diffuse phase-field representation presented in [17] to frictional contact between soft bodies. We propose to include a frictional penalty force field as a function of Eulerian field variables, namely the phase-fields ϕ and the velocities \mathbf{v} of the bodies in contact. Using multiple velocity fields renders the bodies independent, coupled only through contact forces arising from frictional interactions.

We thoroughly validated the method with various numerical examples, demonstrating accuracy by comparison with the analytical Cattaneo-Mindlin solution for frictional contact. Our examples also highlighted the ability to capture history dependence and energy dissipation in frictional contact, respecting the stick-slip transition and providing oscillation-free friction during sliding. We believe that the proposed framework could be employed to complex multi-physical systems where interfacial interactions play a key role.

CRedit authorship contribution statement

Flavio Lorez: Conceptualization, Methodology, Formal analysis, Investigation, Software, Writing - Original Draft, Visualization; **Mohit Pundir:** Conceptualization, Writing - Review & Editing, Supervision, Funding acquisition

Acknowledgments

This work was supported by an ETH Research Grant (24-1 ETH-020). MP acknowledges support from the Swiss National Science Foundation under the SNSF starting grant (TMSGI2.211655). We would also like to thank David S. Kammer and Antoine Sanner for their valuable discussions and insights, which greatly contributed to the development of this work.

Data Availability

The code and generated simulation data from this study have been deposited in the ETH Research Collection database under accession code [\[url will be inserted during the proof process\]](#).

References

- [1] M. B. Amar and M. Wu, "Patterns in biofilms: From contour undulations to fold focussing," *Europhysics Letters*, vol. 108, no. 3, p. 38003, 2014.
- [2] U. M. Angst, "Challenges and opportunities in corrosion of steel in concrete," *Materials and Structures*, vol. 51, no. 1, p. 4, 2018.
- [3] M. Pundir, D. S. Kammer, and U. Angst, "An FFT-based framework for predicting corrosion-driven damage in fractal porous media," *Journal of the Mechanics and Physics of Solids*, vol. 179, p. 105388, 2023.
- [4] V. Yastrebov, "Computational contact mechanics : Geometry , detection and numerical techniques Vladislav Yastrebov To cite this version : HAL Id : Pastel-00657305 École doctorale n O 432 : Sciences des Métiers de l ' Ingénieur THESE l ' École nationale supérieure des mi," 2012.
- [5] J. Li, M. Kothari, S. Chockalingam, T. Henzel, Q. Zhang, X. Li, J. Yan, and T. Cohen, "Nonlinear inclusion theory with application to the growth and morphogenesis of a confined body," *Journal of the Mechanics and Physics of Solids*, vol. 159, p. 104709, 2022.
- [6] J. D. Eshelby and R. E. Peierls, "The elastic field outside an ellipsoidal inclusion," *Proceedings of the Royal Society of London. Series A. Mathematical and Physical Sciences*, vol. 252, no. 1271, pp. 561–569, 1957.
- [7] M. Soleimani, S. P. Szafranski, T. Qu, R. Mukherjee, M. Stiesch, P. Wriggers, and P. Junker, "Numerical and experimental investigation of multi-species bacterial co-aggregation," *Scientific Reports*, vol. 13, no. 1, p. 11839, 2023.
- [8] S. Osher and R. P. Fedkiw, *Level Set Methods and Dynamic Implicit Surfaces*. No. v. 153 in Applied Mathematical Sciences, New York: Springer, 2003.
- [9] Y. Sun and C. Beckermann, "Sharp interface tracking using the phase-field equation," *Journal of Computational Physics*, vol. 220, no. 2, pp. 626–653, 2007.
- [10] W. J. Boettinger, J. A. Warren, C. Beckermann, and A. Karma, "Phase-Field Simulation of Solidification," *Annual Review of Materials Research*, vol. 32, no. 1, pp. 163–194, 2002.
- [11] K. Kamrin, C. H. Rycroft, and J.-C. Nave, "Reference map technique for finite-strain elasticity and fluid–solid interaction," *Journal of the Mechanics and Physics of Solids*, vol. 60, no. 11, pp. 1952–1969, 2012.
- [12] C. H. Rycroft, C.-H. Wu, Y. Yu, and K. Kamrin, "Reference map technique for incompressible fluid–structure interaction," *Journal of Fluid Mechanics*, vol. 898, p. A9, 2020.
- [13] S. Daubner, M. Reder, N. Prajapati, D. Schneider, and B. Nestler, "Multiphase-field modelling of anisotropic elasticity at finite deformation in Eulerian space," *Journal of Computational Science*, vol. 66, p. 101930, 2023.
- [14] B. Valkov, C. H. Rycroft, and K. Kamrin, "Eulerian Method for fluid-structure interaction and submerged solid-solid contact problems," *arXiv*, 2015.
- [15] X. Mao and R. Jaiman, "A 3D phase-field based Eulerian variational framework for multiphase fluid-structure interaction with contact dynamics," 2024.
- [16] B. Rath, X. Mao, and R. K. Jaiman, "An Efficient Phase-field Framework for Contact Dynamics between Deformable Solids in Fluid Flow," 2024.
- [17] F. Lorez, M. Pundir, and D. S. Kammer, "Eulerian framework for contact between solids represented as phase fields," *Computer Methods in Applied Mechanics and Engineering*, vol. 418, p. 116497, 2024.
- [18] Th. Dunne, "An Eulerian approach to fluid–structure interaction and goal-oriented mesh adaptation," *International Journal for Numerical Methods in Fluids*, vol. 51, no. 9-10, pp. 1017–1039, 2006.
- [19] J. W. Cahn and J. E. Hilliard, "Free Energy of a Nonuniform System. I. Interfacial Free Energy," *The Journal of Chemical Physics*, vol. 28, no. 2, pp. 258–267, 1958.

- [20] X. Mao, V. Joshi, and R. Jaiman, “A variational interface-preserving and conservative phase-field method for the surface tension effect in two-phase flows,” *Journal of Computational Physics*, vol. 433, p. 110166, 2021.
- [21] X. Mao and R. Jaiman, “An interface and geometry preserving phase-field method for fully Eulerian fluid-structure interaction,” *Journal of Computational Physics*, vol. 476, p. 111903, 2023.
- [22] X. LI, J. LOWENGRUB, A. RÄTZ, and A. VOIGT, “SOLVING PDES IN COMPLEX GEOMETRIES: A DIFFUSE DOMAIN APPROACH,” *Communications in mathematical sciences*, vol. 7, no. 1, pp. 81–107, 2009.
- [23] S. Aland, “Phase Field Models for Two-Phase Flow with Surfactants and Biomembranes,” in *Transport Processes at Fluidic Interfaces* (D. Bothe and A. Reusken, eds.), Advances in Mathematical Fluid Mechanics, pp. 271–290, Cham: Springer International Publishing, 2017.
- [24] H. Houssein, S. Garnot, and F. Hecht, “Regularized frictional contact problems with the interior point method,” *Japan Journal of Industrial and Applied Mathematics*, vol. 40, no. 2, pp. 775–807, 2023.
- [25] S. Rojas-Labanda and M. Stolpe, “Automatic penalty continuation in structural topology optimization,” *Structural and Multidisciplinary Optimization*, vol. 52, no. 6, pp. 1205–1221, 2015.
- [26] A. Logg, K.-A. Mardal, and G. Wells, eds., *Automated Solution of Differential Equations by the Finite Element Method: The FEniCS Book*, vol. 84 of *Lecture Notes in Computational Science and Engineering*. Berlin, Heidelberg: Springer, 2012.
- [27] S. Balay, S. Abhyankar, M. F. Adams, S. Benson, J. Brown, P. Brune, K. Buschelman, E. M. Constantinescu, L. Dalcin, A. Dener, V. Eijkhout, J. Faibussowitsch, W. D. Gropp, V. Hapla, T. Isaac, P. Jolivet, D. Karpeev, D. Kaushik, M. G. Knepley, F. Kong, S. Kruger, D. A. May, L. C. McInnes, R. T. Mills, L. Mitchell, T. Munson, J. E. Roman, K. Rupp, P. Sanan, J. Sarich, B. F. Smith, S. Zampini, H. Zhang, and J. Zhang, “PETSc/TAO Users Manual (Rev. 3.20),” Tech. Rep. ANL-21/39 Rev. 3-20, Argonne National Laboratory (ANL), Argonne, IL (United States), 2023.
- [28] T. Belytschko, W. K. Liu, B. Moran, and K. Elkhodary, *Nonlinear Finite Elements for Continua and Structures*. John Wiley & Sons, 2014.
- [29] R. D. Mindlin, “Compliance of Elastic Bodies in Contact,” *Journal of Applied Mechanics*, vol. 16, no. 3, pp. 259–268, 1949.
- [30] K. L. Johnson and K. L. Johnson, *Contact Mechanics*. Cambridge University Press, 1987.
- [31] F. J. Cavalieri and A. Cardona, “Numerical solution of frictional contact problems based on a mortar algorithm with an augmented Lagrangian technique,” *Multibody System Dynamics*, vol. 35, no. 4, pp. 353–375, 2015.
- [32] M. A. Puso and T. A. Laursen, “A mortar segment-to-segment frictional contact method for large deformations,” *Computer Methods in Applied Mechanics and Engineering*, vol. 193, no. 45, pp. 4891–4913, 2004.
- [33] L. De Lorenzis, İ. Temizer, P. Wriggers, and G. Zavarise, “A large deformation frictional contact formulation using NURBS-based isogeometric analysis,” *International Journal for Numerical Methods in Engineering*, vol. 87, no. 13, pp. 1278–1300, 2011.
- [34] S. Frei, “Eulerian finite element methods for interface problems and fluid-structure interactions.” <https://archiv.ub.uni-heidelberg.de/volltextserver/21590/>, 2016.
- [35] T. Richter, “A Fully Eulerian formulation for fluid–structure-interaction problems,” *Journal of Computational Physics*, vol. 233, pp. 227–240, 2013.
- [36] D. Mokbel, H. Abels, and S. Aland, “A phase-field model for fluid–structure interaction,” *Journal of Computational Physics*, vol. 372, pp. 823–840, 2018.
- [37] Y. Li, Q. Yu, S. Ham, S. Kwak, C. Lee, and J. Kim, “A phase-field model without artificial curvature effect for the crystal growth simulation,” *International Journal of Heat and Mass Transfer*, vol. 203, p. 123847, 2023.
- [38] S. K. Naghibzadeh, N. Walkington, and K. Dayal, “Surface growth in deformable solids using an Eulerian formulation,” *Journal of the Mechanics and Physics of Solids*, vol. 154, p. 104499, 2021.
- [39] A. M. Jokisaari, P. W. Voorhees, J. E. Guyer, J. A. Warren, and O. G. Heinonen, “Phase field benchmark problems for dendritic growth and linear elasticity,” *Computational Materials Science*, vol. 149, pp. 336–347, 2018.
- [40] H. Sass and A. Reusken, “An accurate and robust Eulerian finite element method for partial differential equations on evolving surfaces,” *Computers & Mathematics with Applications*, vol. 146, pp. 253–270, 2023.
- [41] D. J. Benson and S. Okazawa, “Contact in a multi-material Eulerian finite element formulation,” *Computer Methods in Applied Mechanics and Engineering*, vol. 193, no. 39, pp. 4277–4298, 2004.
- [42] J. R. Rice, N. Lapusta, and K. Ranjith, “Rate and state dependent friction and the stability of sliding between elastically deformable solids,” *Journal of the Mechanics and Physics of Solids*, vol. 49, no. 9, pp. 1865–1898, 2001.
- [43] D. S. Kammer, M. Radiguet, J.-P. Ampuero, and J.-F. Molinari, “Linear elastic fracture mechanics predicts the propagation distance of frictional slip,” *arXiv: Materials Science*, 2014.